TECHNISCHE MECHANIK, Band 26, Heft 1, (2006), 44-64
Manuskripteingang: 28. März 2006

Improved Analytical Modelling of Smart Piezoelectric Beams and its Experimental Verification

J. Dennerlein, U. Gabbert, H. Köppe, S. Nunninger, M. Bechtold

Analytical models can contribute a lot to a better understanding of the structural behaviour of smart structures. In the paper an enhanced analytical model of a cantilever beam is presented. The beam is attached with piezoelectric patches that are used as sensors and actuators in a collocated and a non-collocated manner. In the analysis of the bending vibrations, an Euler-Bernoulli model is combined with a model of the longitudinal vibrations. The mechanical coupling between actuators and collocated sensors is modelled analytically and included in the transfer function as feedthrough. Additionally the model incorporates the effective electromechanical coupling and considers the modelling error due to model truncation. The analytical frequency response functions (FRFs) are verified and compared with experimental data in the frequency range up to 5 kHz including the first 10 bending modes and the first longitudinal mode. The observed differences between the simulated and the measured eigenfrequencies are less than 0.5% except for the first bending and longitudinal mode. The average amplitude modelling error is about 1dB for collocated and about 2dB for non-collocated patch combinations in the frequency range up to 3 kHz.

1 Introduction

In the recent years there has been a growing demand for active vibration control (Gabbert, 2002). In part, this is due to the need for thin and light mechanical structures which, unfortunately, result in undesired vibro-acoustics phenomena. Passive methods for increasing the structural damping are often inadequate, especially in the lower frequency range, and the performance goals can be met only by active vibration control based on distributed piezoelectric actuator and sensor systems. In order to improve the understanding and the modelling of the electromechanical coupling between the piezoelectric patches and the base structure an extensive research has been performed.

Crawley and de Luis (1987) proposed a uniform strain model for surface mounted piezoelectric patches both for longitudinal and bending vibrations. The model incorporated the shear effect of the bonding layer between the patches and the base substrate. Crawley and Anderson (1990) presented an Euler-Bernoulli model for the induced strain assuming consistent Euler-Bernoulli strain over the entire cross-section of the laminate structure.
Exact closed form solutions of the FRF between actuating and sensing piezoelectric patches describing the dynamical behaviour of an Euler-Bernoulli beam were subject of many studies, see e.g. Alberts et. al. (1995), Pota and Alberts (1995), Preumont (2002) and Stöbener (2002). In general this analytical approach is applied only to simple models that are valid just for low frequency ranges and low modal orders. Usually complex models for higher frequency ranges are implemented using the finite element (FE) modelling, see e.g. Kusculuoglu et. al. (2004) and Nguyen and Pietrzko (2004).
Maxwell and Asokanthan (2004) investigated the effect of surface mounted piezoelectric patches on the modal characteristics of a cantilever Timoshenko beam. The effect of model reduction errors, termed residual mode, on the modelling of FRFs was discussed by Gao and Randall (1996). Similar to the residual mode is the influence of the mechanical coupling between actuating and collocated sensing piezoelectric patches on the FRFs. Alvarez-Salazar and Iliff (1999) determined the coupling by measurement and included it in the transfer function (TF) as an additional constant, called feedthrough.

In the present work the traditional closed form solutions for the bending vibrations of an Euler-Bernoulli beam with surface mounted piezoelectric patches are revised and combined with a model for the longitudinal vibrations. A novel methodology is introduced to model analytically the mechanical coupling between actuating and collocated sensing patches based on the strain and stress distributions of the active and passive beam layers. Furthermore the effective electromechanical coupling and the modelling error due to model truncation are

discussed. A new enhanced analytical beam model is proposed in modal form. Additionally, the analytically calculated FRFs are verified and compared with numerically simulated and experimentally measured ones in a frequency range extended to higher frequencies and modal orders.

2 Assumptions

A thin, rectangular and isotropic cantilever beam as shown in Figure 1 is considered. Four identical piezoelectric patches are supposed to be perfectly and symmetrically surface mounted in a collocated and non-collocated manner on both sides of the beam. The patches can be used as actuators or sensors. In the following the super- or subscript b denotes the beam and the super- or subscript p the patches.

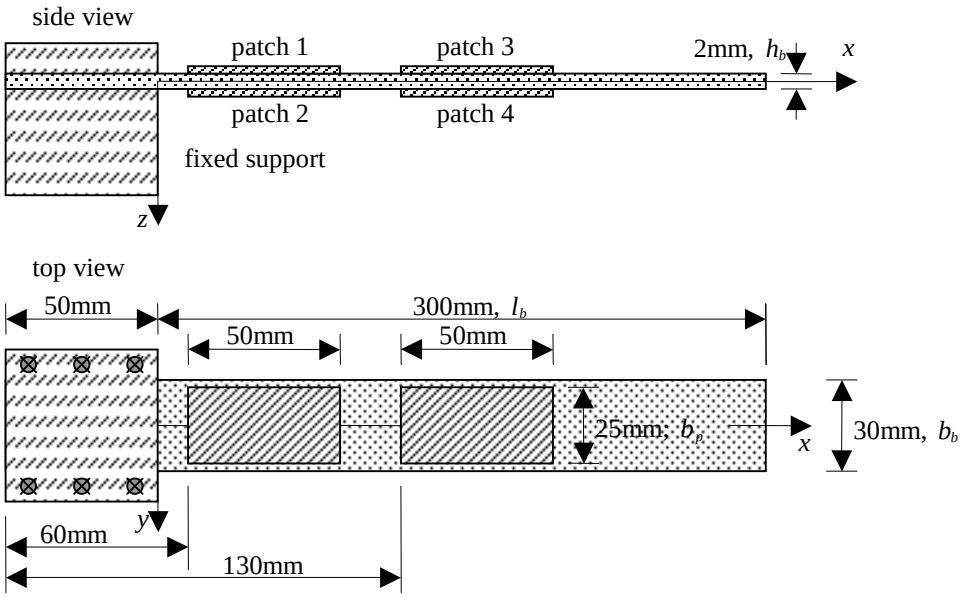

Figure 1. Geometry and layout of the cantilever beam with surface mounted piezoelectric patches

The beam is made of steel type St05Z and the piezoelectric patches are made of Lead-Zirkonate-Titanate (PZT) ceramic type Sonox P53. The principal characteristics of both materials are listed in Table 1. The positioning of the patches is based on the results of (BMBF, 1998), where the placement for the active vibration control of beams is discussed.

	steel St05Z	Sonox P53
$l \times b \times h$ [10^{-3} m]	300 x 30 x 2	50 x 25 x 0.2
ρ_p [kg/m^3]	7850	7830
E [10^9 N/m^2]	198	67
ν_{13}, ν_{23}	0.33	0.34
d_{31}, d_{32} [10^{-12} m/V]	---	-233
e_{31}, e_{32} [N/Vm]	---	-15.3
ε_r	---	1630

Table 1. Characteristics of steel St05Z and Sonox P53 (BMBF, 1998)

The origin of the coordinate system is located in the middle at the fixed end of the beam, see Figure 1. Due to the symmetry of the beam and the piezoelectric patches the longitudinal displacement $u(x,t)$ and the bending displacement $w(x,t)$ are uncoupled and can be analysed separately (Edery-Azulay and Abramovich, accepted).

It is assumed that the mass and the stiffness of the piezoelectric patches can be neglected in comparison with the mass and the bending stiffness of the beam (Maxwell and Asokanthan, 2004). Because of the length to the thickness ratio of the patches the edge effects of the patches can be ignored. In the analysis the bonding layer is supposed to be plane and thin such that it has not to be considered (Crawley and de Luis, 1987). An Euler-Bernoulli model is used, neglecting the rotary inertia and shear deformation of the beam.

3 Longitudinal Vibration

An element of the beam undergoing pure longitudinal displacements is shown in Figure 2.

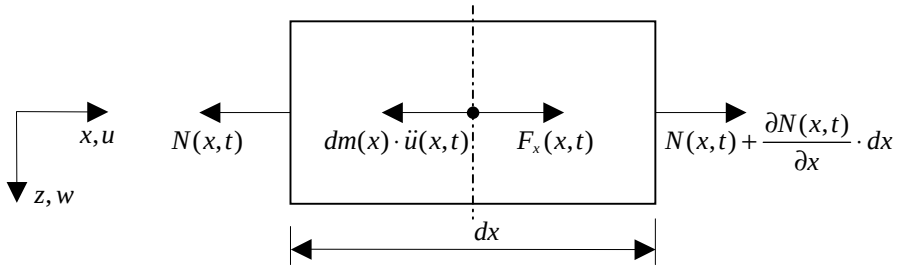

Figure 2. Beam element in longitudinal motion

3.1 Differential Equation of Motion

Applying the condition of force equilibrium in the x direction results in

$$\frac{\partial N_x(x,t)}{\partial x} \cdot dx - dm(x) \cdot \ddot{u}(x,t) = -F_x(x,t) \cdot dx \tag{1}$$

where $N_x(x,t)$ is the internal force, $F_x(x,t)$ is the external axial force, $dm(x,t)$ is the element mass of the beam element while $u(x,t)$ is the longitudinal displacement. Substituting the relation for the mass, $dm(x) = \rho_b(x) \cdot A_b(x) \cdot dx$, and the internal force applying the Hook's law, $N_x(x,t) = E_b(x) \cdot A_b(x) \cdot u'(x,t)$, into equation (1) one obtains the differential equation of motion as (Meyers, 2005)

$$[E_b(x) \cdot A_b(x) \cdot u'(x,t)]' - \rho_b(x) \cdot A_b(x) \cdot \ddot{u}(x,t) = -F_x(x,t) \tag{2}$$

where $E_b(x)$ is the Young's modulus of the beam, $A_b(x)$ is the cross section of the beam and $\rho_b(x)$ is the mass density.

3.2 Solution of the Differential Equation of Motion

The homogenous differential equation of motion is solved using separation of variables. The general solution considers both location and time dependency of the displacement $u(x,t)$ and can be expressed as

$$u(x,t) = U(x) \cdot \eta(t) \tag{3}$$

where $U(x)$ is the spatial mode shape function and $\eta(t)$ is the time dependency. By substitution of equation (3) into equation (2) and assuming constant values for the mass density ρ_b, the Young's modulus E_b and the cross sectional area A_b one finds the homogenous spatial differential equation which can be written as

$$U''(x) - \beta^2 \cdot U(x) = 0 \tag{4}$$

with the abbreviation

$$\beta^2 = \rho_b / E_b \cdot \omega^2 \tag{5}$$

The eigenvalues $\pm j \cdot \beta$ of the equation (4) define the general solution of the mode shape $U(x)$ given by

$$U(x) = \hat{C}_1 \cdot \cos(\beta \cdot x) + \hat{C}_2 \cdot \sin(\beta \cdot x) \tag{6}$$

where $\hat{C}_1$ and $\hat{C}_2$ are constants. The cantilever beam is clamped at one end and free at the other end. With these assumptions the displacement $U(x)$ is constrained to zero at the fixed end $x = 0$

$$U(0) = 0 \tag{7}$$

and the internal force $N_x(x)$ is constrained to zero at the free end $x = l_b$

$$N_x(l_b) = A_b \cdot E_b \cdot \partial U(x) / \partial x\big|_{x=l_b} = 0 \tag{8}$$

Applying equation (6) to equations (7) and (8) the characteristic equation is derived which results in

$$\cos(\beta \cdot l_b) = 0 \tag{9}$$

The solutions of the characteristic equation are written in the form

$$\beta_i = \frac{\pi}{2 \cdot l_b} \cdot (2 \cdot i - 1), \quad i = 1, 2, 3, \ldots \tag{10}$$

Introducing equation (10) into equation (6) and applying the boundary conditions (7) and (8) one can derive the mode shape $U_i(x)$ as shown in Figure 3 and given by (Meyers, 2005)

$$U_i(x) = -\hat{C}_i^u \cdot \sin\left(\frac{\pi}{2 \cdot l_b} \cdot (2 \cdot i - 1) \cdot x\right) \tag{11}$$

To ease further calculations the mode shape $U_i(x)$ is normalised by an orthonormality condition. The condition is obtained by multiplying the differential equations of motion (4) for the eigenvalues β_i and β_j respectively with the mode shapes $U_j(x)$ and $U_i(x)$ respectively, subsequent subtraction of the equations and integration over the length l_b. The orthonormality condition is given in the form

$$\int_{l_b} \rho_b(x) \cdot A_b(x) \cdot U_i(x) \cdot U_j(x)\, dx = \delta_{ij}, \quad \delta_{ij} = \begin{cases} 0 & \text{for } i \neq j \\ 1 & \text{for } i = j \end{cases} \tag{12}$$

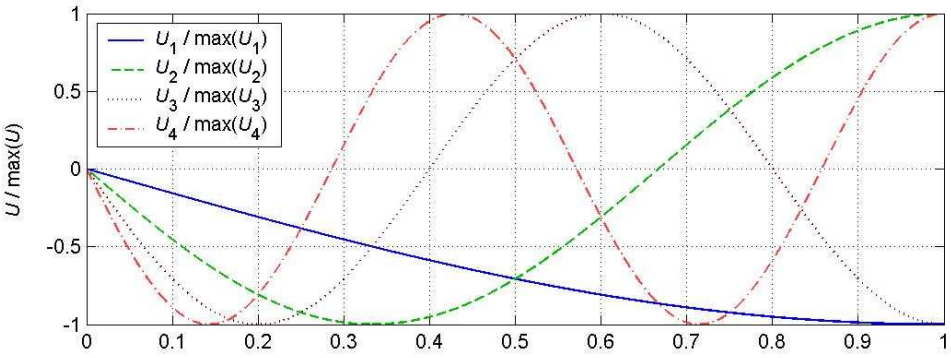

Figure 3. Mode shapes of the longitudinal vibration

4 Bending Vibration

An element of the beam undergoing pure bending displacements is shown in Figure 4.

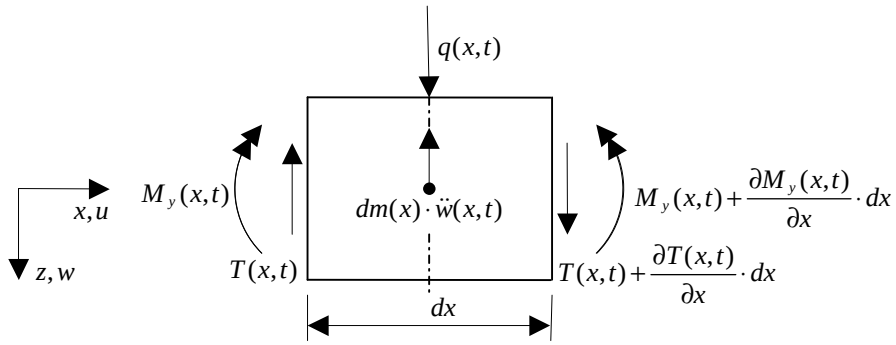

Figure 4. Beam element in transverse motion

4.1 Differential Equation of Motion

Balancing the forces in z direction and the bending moments around the centre of the beam while neglecting the bending moments of higher order terms results in

$$\frac{\partial T(x,t)}{\partial x}\cdot dx = dm(x)\cdot \ddot{w}(x,t) - q(x,t) \tag{13}$$

$$\frac{\partial M_y(x,t)}{\partial x}\cdot dx = T(x,t)\cdot dx \tag{14}$$

where $q(x,t)$ is the external load force. Introducing the relation of the finite element mass, $dm(x) = \rho_b(x)\cdot A_b(x)\cdot dx$, and of the bending moment, $M_y(x,t) = -E_b(x)\cdot I_{yy}(x)\cdot w''(x,t)$, into equations (13) and (14) we derive the differential equation of motion as (Meyers, 2005)

$$[E_b(x)\cdot I_{yy}(x)\cdot w''(x,t)]'' + \rho_b(x)\cdot A_b(x)\cdot \ddot{w}(x,t) = q(x,t) \tag{15}$$

where $I_{yy}(x)$ is the moment of inertia.

4.2 Solution of the Differential Equation of Motion

Following the previous approach of the section 3.2 the bending vibration $w(x,t)$ is written as

$$w(x,t) = W(x) \cdot \eta(t) \tag{16}$$

where $W(x)$ is the spatial mode shape function. Substituting equation (16) into equation (15) and assuming constant values for the mass density ρ_b, the Young's modulus E_b, the cross sectional area A_b and the moment of inertia $I_{yy}(x)$ the homogenous spatial differential equation can be determined as

$$W''''(x) - \beta^4 \cdot W(x) = 0 \tag{17}$$

with the abbreviation

$$\beta^4 = \omega^2 \cdot \frac{\rho_b \cdot A_b}{E_b \cdot I_{yy}} \tag{18}$$

The general solution of the mode shape $W(x)$

$$W(x) = \hat{C}_1 \cdot \sin(\beta \cdot x) + \hat{C}_2 \cdot \cos(\beta \cdot x) + \hat{C}_3 \cdot \sinh(\beta \cdot x) + \hat{C}_4 \cdot \cosh(\beta \cdot x) \tag{19}$$

is combined with the boundary conditions at the clamped end $x = 0$

$$W(x = l_b) = 0 \text{ and } \left.\frac{\partial W(x)}{\partial x}\right|_{x=l_b} = 0 \tag{20}$$

and the boundary conditions at the free end $x = l_b$

$$M_y(l_b) = -E_b \cdot I_{yy} \cdot \left.\frac{\partial^2 W(x)}{\partial x^2}\right|_{x=l_b} = 0 \text{ and } T(l_b) = -E_b(x) \cdot I_{yy} \cdot \left.\frac{\partial^3 W(x)}{\partial x^3}\right|_{x=l_b} = 0 \tag{21}$$

resulting in the characteristic equation which can be expressed by

$$1 + \cos(\beta \cdot l_b) \cdot \cosh(\beta \cdot l_b) = 0 \tag{22}$$

The characteristic values of the equation (22) are computed numerically as follows

$$\beta_1 \cdot l_b = 1.8751, \beta_2 \cdot l_b = 4.6941, \beta_3 \cdot l_b = 7.8548, \beta_i \cdot l_b \approx (2 \cdot i - 1) \cdot \pi / 2, \quad i > 3 \tag{23}$$

Substituting equation (23) into equation (19) and considering the boundary conditions (20) and (21) we can determine the mode shape $W_i(x)$ as shown in Figure 5 and given by (Nguyen and Pietrzko, 2004)

$$W_i(x) = -\hat{C}_i^w \cdot [(\cos(\beta_i \cdot x) - \cosh(\beta_i \cdot x)) + \alpha \cdot (\sin(\beta_i \cdot x) - \sinh(\beta_i \cdot x))] \tag{24}$$

where

$$\alpha = \frac{\sin(\beta_i \cdot l_b) - \sinh(\beta_i \cdot l_b)}{\cos(\beta_i \cdot l_b) + \cosh(\beta_i \cdot l_b)} \tag{25}$$

As before the mode shape $W_i(x)$ is normalised by the orthonormality condition that is given by

$$\int_{l_b} \rho_b(x) \cdot A_b(x) \cdot W_i(x) \cdot W_j(x)\, dx = \delta_{ij}, \quad \delta_{ij} = \begin{cases} 0 & \text{for } i \neq j \\ 1 & \text{for } i = j \end{cases} \tag{26}$$

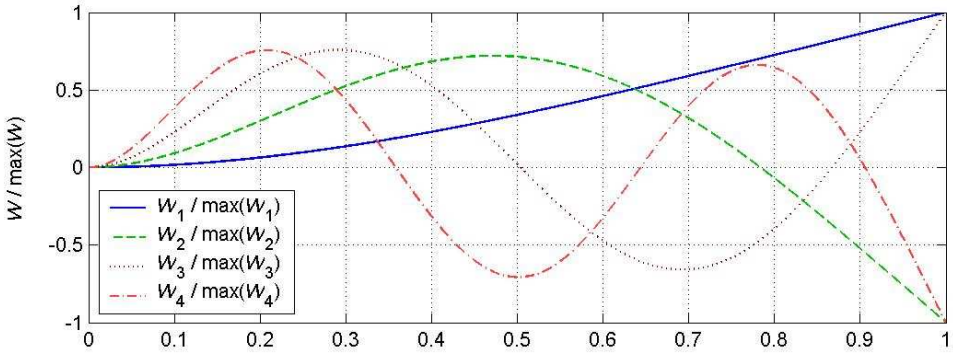

Figure 5. Mode shapes of the bending vibration

5 Patch Actuator

The patch consists of a piezoelectric layer made of PZT ceramic that is covered with thin Silver electrodes on the upper and lower side, see Figure 6. The PZT ceramic is polarised in z direction. Applying voltage $V(t)$ across the actuating patch in direction of the polarisation P induces a stress $\sigma_x(t)$ within the layer in x direction. In case the displacement of the patch is constraint to zero the stress $\sigma_x(t)$ can be written as

$$\sigma_x(t) = E_p \cdot d_{31} \cdot \frac{1}{h_p} \cdot V(t) \tag{27}$$

where d_{31} is the piezoelectric constant, E_p is the Young's modulus of the patch while h_p is the height.

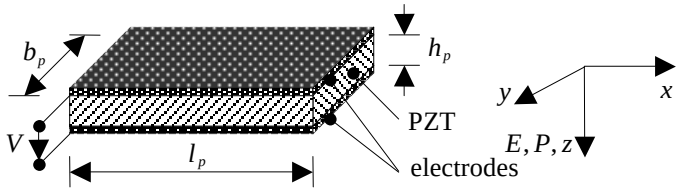

Figure 6. Geometry and layout of the patch

Integrating the stress $\sigma_x(t)$ over the height h_p yields the resulting distributed force $F_x(t)$ within the layer.

$$F_x(t) = \int_{\frac{h_b}{2}}^{\frac{h_b}{2}+h_p} \sigma_x(t) dz = E_p \cdot d_{31} \cdot V(t) \tag{28}$$

where h_b is the height of the beam. The distributed force $F_x(x,t)$ acts only on the edges of the patch as illustrated in Figure 7.

$$F_x(x,t) = F_x(t) \cdot [\delta_0(x - x_2) - \delta_0(x - x_1)] \cdot [\delta_1(y - y_1) - \delta_1(y - y_2)] \tag{29}$$

where δ_0 is the delta function, δ_1 is the step function, x_1, x_2, y_1 and y_2 are the location coordinates of the patch. The point force $F_x(t)$ in turn generates a bending moment $M_y(t)$ about the neutral axis of the beam.

$$M_y(t) = \int_{\frac{h_b}{2}}^{\frac{h_b}{2}+h_p} \sigma_x(t) \cdot z dz = \frac{1}{2} \cdot E_p \cdot d_{31} \cdot (h_b + h_p) \cdot V(t) \tag{30}$$

Once again the bending moment $M_y(x,t)$ acts only on the edges of the patch (Fuller et. al., 1997).

$$M_y(x,t) = M_y(t) \cdot [\delta_0(x - x_2) - \delta_0(x - x_1)] \cdot [\delta_1(y - y_1) - \delta_1(y - y_2)] \tag{31}$$

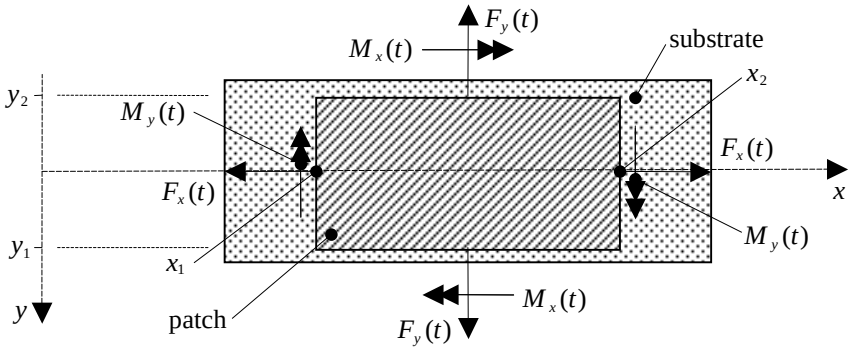

Figure 7. Forces and bending moments of piezoelectric patch

The modal input gain of the actuating patch is given by the generalised modal work $\tilde{N}_i(x,t)$ carried out in the mode shapes (Preumont, 2002). For the longitudinal vibration the work $\tilde{N}_i^u(x,t)$ is performed by the distributed force $F_x(x,t)$ in the mode shape $U_i(x)$ and can be derived as

$$\tilde{N}_i^u(x,t) = \int_{A_p} [U_i(x) \cdot F_x(x,t)]\, dA = E_p \cdot d_{31} \cdot b_p \cdot [U_i(x_2) - U_i(x_1)] \cdot V(t) \tag{32}$$

where b_p is the width of the patch. Similarly, for the bending vibration the generalised modal work $\tilde{N}_i^w(x,t)$ is produced by the bending moment $M_y(x,t)$ in the mode shape $W_i(x)$ and is obtained as

$$\tilde{N}_i^w(x,t) = \int_{A_p} [\varphi_i(x) \cdot M_y(x,t)]\, dA = -\frac{1}{2} \cdot E_p \cdot d_{31} \cdot (h_b + h_p) \cdot b_p \cdot \left[\frac{\partial W_i(x_2)}{\partial x} - \frac{\partial W_i(x_1)}{\partial x} \right] \cdot V(t) \tag{33}$$

The same procedure can be applied for the y direction which is not considered here.

6 Patch Sensor

Next, the voltage across the sensing patch is calculated. The strain $\varepsilon_{xi}^u(x,t)$ of the pure longitudinal deformation is given by the first derivation of the mode shape $u_i(x,t)$ as

$$\varepsilon_{xi}^u(x,t) = \frac{\partial u_i(x,t)}{\partial x} \tag{34}$$

In case of the pure bending deformation the strain $\varepsilon_{xi}^{w}(x,t)$ is proportional to the curvature of the beam and the transverse coordinate z and can be expressed as

$$\varepsilon_{xi}^{w}(x,t) = -\frac{h_b + h_p}{2} \cdot \frac{\partial^2 w_i(x,t)}{\partial x^2} \tag{35}$$

The electric displacement $D_i(x,t)$ is related to the strain $\varepsilon_{xi}(x,t)$ and is given by

$$D_i(x,t) = e_{31} \cdot \varepsilon_{xi}(x,t) \tag{36}$$

where e_{31} is the piezoelectric charge density. The modal output gain of the sensing patch is given by the generalised modal charge $Q_i(t)$ generated by the mode shapes (Preumont, 2002). Integration of the electric displacement $D_i(x,t)$ over the active area of the patch gives the modal charge $Q_i(t)$. For the longitudinal vibration this results in

$$Q_i^u(x,t) = -\int_{A_p} D_i^u(x,t)dA = -e_{31} \cdot b_p \cdot [u_i(x_2,t) - u_i(x_1,t)] \tag{37}$$

and for the bending vibration one obtains

$$Q_i^w(x,t) = -\int_{A_p} D_i^w(x,t)dA = \frac{1}{2} \cdot e_{31} \cdot b_p \cdot (h_b + h_p) \cdot \left[\frac{\partial w_i(x_2,t)}{\partial x} - \frac{\partial w_i(x_1,t)}{\partial x} \right] \tag{38}$$

Assuming the patch is similar to an ideal electric parallel plate capacitor the resulting generalised modal voltage $V_i^u(x,t)$ for the longitudinal vibration is given by

$$V_i^u(x,t) = \frac{Q_i^u(x,t)}{C} = -\frac{1}{\varepsilon_0 \cdot \varepsilon_r} \cdot e_{31} \cdot \frac{h_p}{l_p} \cdot [u_i(x_2,t) - u_i(x_1,t)] \tag{39}$$

where C is the capacitance of the patch, ε_0 is the permittivity of free space, ε_r is the relative permittivity of the piezoelectric layer and l_p is the length of the patch. Likewise the generalised modal voltage $V_i^w(x,t)$ for the bending vibration is calculated by

$$V_i^w(x,t) = \frac{Q_i^w(x,t)}{C} = \frac{1}{2} \cdot \frac{1}{\varepsilon_0 \cdot \varepsilon_r} \cdot e_{31} \cdot \frac{(h_b + h_p) \cdot h_p}{l_p} \cdot \left[\frac{\partial w_i(x_2,t)}{\partial x} - \frac{\partial w_i(x_1,t)}{\partial x} \right] \tag{40}$$

7 Strains and Stresses

A collocated patch configuration is shown in Figure 8. In the following the strain and stress distributions within the beam for an asymmetric excitation with the upper patch is derived. The approach is based on the work of Fuller et. al. (1997) but includes the additional layer of the collocated sensing patch. An important assumption is that the patch is thin and lightweight so that the inertia effects can be neglected. The bonding layer is ignored, which is valid if the layer is plane and thin. In the following analysis only the x direction is considered but the results are valid also for the y direction. The super- or subscripts pa denote the actuating patch while the super- or subscripts ps denote the sensing patch.

Applying voltage $V(t)$ across the actuating patch causes the unconstrained patch to strain in x direction by

$$\varepsilon_x^{pa}(t) = d_{31} \cdot \frac{1}{h_p} \cdot V(t) \tag{41}$$

Considering however a bonded patch this will try to expand but is constrained by the stiffness of the beam. Due to the asymmetric load the beam will both expand and bend producing an asymmetric strain distribution as shown in Figure 8. Based on the Euler-Bernoulli hypothesis we can assume a linear strain distribution in the xz plane that can be written as

$$\varepsilon_x(z,t) = C_x(t) \cdot z + \hat{\varepsilon}_x(t) \tag{42}$$

where $C_x(t)$ is the slope and $\hat{\varepsilon}_x(t)$ is the point of interception with the z axis.

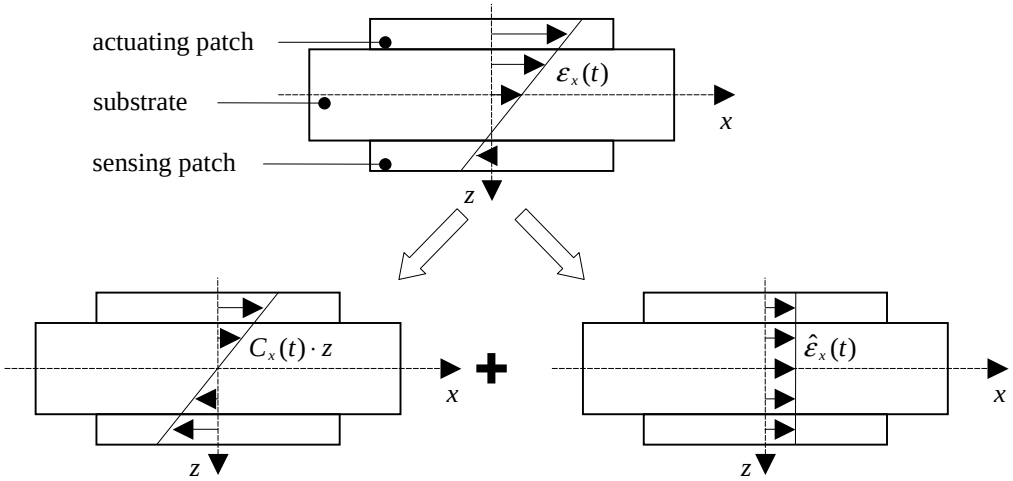

Figure 8. Asymmetric strain distribution

The stress distribution $\sigma_x^{pa}(z,t)$ within the actuating patch is made up of the unconstrained patch strains $\varepsilon_x^{pa}(t)$ and $\varepsilon_y^{pa}(t)$ and the assumed linear strain distributions $\varepsilon_x(z,t)$ and $\varepsilon_y(z,t)$. Using Hook's law the stress distribution $\sigma_x^{pa}(z,t)$ can be expressed as

$$\sigma_x^{pa}(z,t) = \frac{E_x^p}{1-\nu_p^2} \cdot [C_x(t) \cdot z + \hat{\varepsilon}_x(t) + \nu_p \cdot (C_y(t) \cdot z + \hat{\varepsilon}_y(t)) - (\varepsilon_x^{pa}(t) + \nu_p \cdot \varepsilon_y^{pa}(t))] \tag{43}$$

where E_x^p is the Young's modulus of the patch while ν_p is the Poisson ratio. Respectively, the stress distribution $\sigma_x^b(z,t)$ within the beam substrate is given by

$$\sigma_x^b(z,t) = \frac{E_x^b}{1-\nu_b^2} \cdot [C_x(t) \cdot z + \hat{\varepsilon}_x(t) + \nu_b \cdot (C_y(t) \cdot z + \hat{\varepsilon}_y(t))] \tag{44}$$

where E_x^b is the Young's modulus of the beam substrate while ν_b is the Poisson ratio. The stress distribution $\sigma_x^{ps}(z,t)$ within the sensing patch is written as

$$\sigma_x^{ps}(z,t) = \frac{E_{11}^p}{1-\nu_p^2} \cdot [C_x(t) \cdot z + \hat{\varepsilon}_x(t) + \nu_p \cdot (C_y(t) \cdot z + \hat{\varepsilon}_y(t))] \tag{45}$$

The further analysis is simplified by the isotropic substrate properties of the patch. The identical piezoelectric constants d_{31} and d_{32} impose equal strains

$$\varepsilon_{pa}(t) = \varepsilon_x^{pa}(t) = \varepsilon_y^{pa}(t) \tag{46}$$

in x and y direction. The substrate of the beam has nearly similar Young's modules in both in-plane directions (BMBF, 1998).

$$E_x^b / E_y^b = 1.02 \Rightarrow E_b \approx E_x^b \approx E_y^b \tag{47}$$

Together with the identical Young's modules E_x^p and E_y^p of the patch this enforces equal stress and strain distributions

$$\sigma_{pa}(z,t) = \sigma_x^{pa}(z,t) = \sigma_y^{pa}(z,t) \tag{48}$$

$$\sigma_b(z,t) = \sigma_x^b(z,t) = \sigma_y^b(z,t) \tag{49}$$

$$\sigma_{ps}(z,t) = \sigma_x^{ps}(z,t) = \sigma_y^{ps}(z,t) \tag{50}$$

$$\varepsilon(z,t) = \varepsilon_x(z,t) = \varepsilon_y(z,t) \tag{51}$$

in x and y direction. Furthermore the Poisson's ratio ν_p of the patches and ν_b of the beam substrate is nearly the same

$$\nu_b / \nu_p = 0.97 \Rightarrow \nu \approx \nu_b \approx \nu_p \tag{52}$$

such that the Poisson's ratio ν can be replaced in equations (43), (44) and (45) resulting in

$$\sigma_{pa}(z,t) = \frac{E_p}{1-\nu} \cdot [C(t) \cdot z + \hat{\varepsilon}(t) - \varepsilon_{pa}(t)] \tag{53}$$

$$\sigma_b(z,t) = \frac{E_b}{1-\nu} \cdot [C(t) \cdot z + \hat{\varepsilon}(t)] \tag{54}$$

$$\sigma_{ps}(z,t) = \frac{E_p}{1-\nu} \cdot [C(t) \cdot z + \hat{\varepsilon}(t)] \tag{55}$$

Employing the force equilibrium in x direction results in the relation

$$\int_{-h_p-\frac{h_b}{2}}^{-\frac{h_b}{2}} \sigma_{ps}(z,t)\, dz + \int_{-\frac{h_b}{2}}^{+\frac{h_b}{2}} \sigma_b(z,t)\, dz + \int_{+\frac{h_b}{2}}^{+\frac{h_b}{2}+h_p} \sigma_{pa}(z,t)\, dz = 0 \tag{56}$$

and the moment equilibrium about the centre of the beam gives the condition

$$\int_{-h_p-\frac{h_b}{2}}^{-\frac{h_b}{2}} \sigma_{ps}(z,t) \cdot z\, dz + \int_{-\frac{h_b}{2}}^{+\frac{h_b}{2}} \sigma_b(z,t) \cdot z\, dz + \int_{+\frac{h_b}{2}}^{+\frac{h_b}{2}+h_p} \sigma_{pa}(z,t) \cdot z\, dz = 0 \tag{57}$$

The equations (56) and (57) are integrated and solved for the unknowns $C(t)$ and $\hat{\varepsilon}(t)$. Finally, we obtain the slope $C(t)$ and the interception $\hat{\varepsilon}(t)$ of the Euler-Bernoulli strain which are expressed by

$$\hat{\varepsilon}(t) = \underbrace{\frac{E_p \cdot h_p}{2 \cdot E_p \cdot h_p + E_b \cdot h_b}}_{K_u} \cdot \varepsilon_{pa}(t) = K_u \cdot \varepsilon_{pa}(t) \tag{58}$$

$$C(t) = \underbrace{\frac{6 \cdot E_p \cdot h_p \cdot (h_b + h_p)}{E_b \cdot h_b^3 + 6 \cdot E_p \cdot h_b^2 \cdot h_p + 12 \cdot E_p \cdot h_b \cdot h_p^2 + 8 \cdot E_p \cdot h_p^3}}_{K_w} \cdot \varepsilon_{pa}(t) = K_w \cdot \varepsilon_{pa}(t) \tag{59}$$

8 Actuator Sensor Coupling

Following the strain distribution analysis we now derive an expression for the mechanical coupling K_D, called feedthrough, between actuating and collocated sensing patch. In general the Euler-Bernoulli beam is considered to be a one dimensional system with bending and longitudinal displacements only in the xz plane and along the x axis respectively (Fuller et. al., 1997). The discussion in the section 7 showed that this assumption is not valid in the close surrounding of the actuating patch. The electric displacement $D(x,t)$ in the sensing patch caused by the strain $\varepsilon(z,t)$ in the xz and yz plane is given by

$$D(z,t) = 2 \cdot e_{31} \cdot d_{31} \cdot \frac{(K_w \cdot z + K_u)}{h_p} \cdot V_{pa}(t) \tag{60}$$

where $V_{pa}(t)$ is the voltage applied across to the actuating patch. Integrating the electric displacement $D(x,t)$ over the active area of the sensing patch one obtains the charge $Q(t)$ generated by the mechanical coupling which can be written as

$$Q(t) = -\int_{A_p} D(z,t)\, dA = -2 \cdot e_{31} \cdot d_{31} \cdot \left(-K_w \cdot \frac{h_b + h_p}{2} + K_u \right) \cdot \frac{l_p \cdot b_p}{h_p} \cdot V_{pa}(t) \tag{61}$$

The resulting voltage $V_{ps}(t)$ of the sensing piezoelectric patch is given by

$$V_{ps}(t) = \frac{Q(t)}{C} = \underbrace{-2 \cdot \frac{1}{\varepsilon_0 \cdot \varepsilon_r} \cdot e_{31} \cdot d_{31} \cdot \left(-K_w \cdot \frac{h_b + h_p}{2} + K_u \right)}_{K_D} \cdot V_{pa}(t) \tag{62}$$

9 Effective Coupling Factor

The polarisation P of a piezoelectric layer reduces gradually with time after polarisation resulting in a decreased piezoelectric constant d_{31} and a degraded piezoelectric charge density e_{31}. Typically the coupling coefficient of low-voltage PZTs decreases by 0.5% to 2% per unit time decade while the coupling coefficient of high-voltage PZTs decreases by 1% to 4%, see (PI Ceramic GmbH, 2005a) and (CeramTec, 2006). Mishandling the element by exceeding its electrical, mechanical or thermal limitations accelerates the aging process.
In addition the manufacturing tolerances of the type of patches used for the functional demonstrator are typically up to $\pm 0.25\text{mm}$ regarding the length l_p and width b_p of the patch (PI Ceramic GmbH, 2005b). Both the thickness h_p and the dielectric properties d_{31} and e_{31} of the patches are within $\pm 10\%$ of the specified values.

The effective electromechanical properties are taken into account by an effective coupling factor K_{eff}.

$$d_{31}^{eff} = K_{eff} \cdot d_{31} \tag{63}$$

$$e_{31}^{eff} = K_{eff} \cdot e_{31} \tag{64}$$

10 Analytical Frequency Response Function and Residual Mode

The Euler-Bernoulli beam is theoretically a system of infinite modal order. The FRF of such a system is written in the pole-residue representation as follows

$$H(\omega) = \sum_{i=1}^{\infty} \frac{R_i}{(j \cdot \omega - s_{pi}) \cdot (j \cdot \omega - s_{pi}^*)} \tag{65}$$

where R_i is the residue of the mode i while s_{pi} is the complex pole in the s plane and * means the complex conjugate. In principle the sum extends to all modes of the system. One obtains a reduced order model by truncation of the model above the frequency range of interest (Wang, 1998), (Randall and Gao, 1994)

$$H(\omega) = \underbrace{\sum_{i=1}^{n_p} \frac{R_i}{(j\cdot\omega - s_{pi})\cdot(j\cdot\omega - s_{pi}^*)}}_{\text{in-of-band modes}} + \underbrace{\sum_{i=n_p+1}^{\infty} \frac{R_i}{(j\cdot\omega - s_{pi})\cdot(j\cdot\omega - s_{pi}^*)}}_{\text{out-of-band modes}} \tag{66}$$

which can also be written in the form

$$H(\omega) = H_{in}(\omega) + H_{out}(\omega) \tag{67}$$

The out-of-band FRF $H_{out}(\omega)$ is called residual mode. The anti-resonances of the reduced order model are the zeros of the FRF $H_{in}(\omega)$. In general they differ from the anti-resonances of the full order model $H(\omega)$ determined by the zeros of the sum $H_{in}(\omega) + H_{in}(\omega)$.
Furthermore the residual mode influences the magnitude and phase of the FRF. The contribution of the residual mode to the FRF can be written as (Gao and Randall, 1996)

$$K_R(\omega) = 20\cdot\sum_{i=n_z+1}^{\infty}\log_{10}(|(j\cdot\omega - s_{zi})\cdot(j\cdot\omega - s_{zi}^*)|) - 20\cdot\sum_{i=n_p+1}^{\infty}\log_{10}(|(j\cdot\omega - s_{pi})\cdot(j\cdot\omega - s_{pi}^*)|) \tag{68}$$

where s_{zi} and s_{pi} are the complex zeros and poles of the transfer function $H_{out}(\omega)$. The frequency dependency of $K_R(\omega)$ within the in-band range essentially depends on the ratio of the zeros and poles. At best the actuating and sensing patches are arranged in a collocated manner such that the resulting FRF has alternating zeros and poles. As a consequence of the interlacing pattern the contribution of a pole s_{pi} is compensated for by the contribution of the subsequent zero s_{zi} and $K_R(\omega)$ is nearly constant.
The greater is the distance between the actuating and sensing patch the less is the number of FRF zeros (Gao and Randall, 1996) and the greater is the frequency dependency of $K_R(\omega)$. In the worst case with patches placed on the opposite sides of the beam there may be no zeros at all (Randall and Gao, 1994).

11 Finite Element Formulation and Frequency Response Function

The finite element model of a general flexible structure can be written in nodal degrees of freedom by a second order matrix differential equation (Gabbert et. al., 2000), (Görnandt and Gabbert, 2002) as

$$\mathbf{M}\cdot\ddot{\mathbf{q}} + \mathbf{D}\cdot\dot{\mathbf{q}} + \mathbf{K}\cdot\mathbf{q} = \hat{\mathbf{B}}\cdot\mathbf{u} \tag{69}$$

$$\mathbf{y} = \hat{\mathbf{C}}\cdot\mathbf{q} \tag{70}$$

where $\mathbf{q}$, $\dot{\mathbf{q}}$ and $\ddot{\mathbf{q}}$ are the nodal displacement, velocity and acceleration vectors, $\mathbf{M}$, $\mathbf{D}$ and $\mathbf{K}$ are the mass, damping and stiffness matrices, $\hat{\mathbf{B}}$ is the input matrix, $\hat{\mathbf{C}}$ is the output matrix and $\mathbf{u}$ and $\mathbf{y}$ are the input and output vector respectively. Introducing the variable $\mathbf{q} = \mathbf{\Phi}\cdot\mathbf{q}_m$ one obtains the model in modal coordinates

$$\underbrace{\mathbf{\Phi}^T\cdot\mathbf{M}\cdot\mathbf{\Phi}}_{\mathbf{M}_m}\cdot\ddot{\mathbf{q}}_m + \underbrace{\mathbf{\Phi}^T\cdot\mathbf{D}\cdot\mathbf{\Phi}}_{\mathbf{D}_m}\cdot\dot{\mathbf{q}}_m + \underbrace{\mathbf{\Phi}^T\cdot\mathbf{K}\cdot\mathbf{\Phi}}_{\mathbf{K}_m}\cdot\mathbf{q}_m = \underbrace{\mathbf{\Phi}^T\cdot\hat{\mathbf{B}}}_{\hat{\mathbf{B}}_m}\cdot\mathbf{u} \tag{71}$$

$$\mathbf{y} = \underbrace{\hat{\mathbf{C}}\cdot\mathbf{\Phi}^T}_{\hat{\mathbf{C}}_m}\cdot\mathbf{q}_m \tag{72}$$

where $\mathbf{\Phi}$ is the matrix of mode shapes and $\hat{\mathbf{B}}_m$ and $\hat{\mathbf{C}}_m$ is the modal input and output matrix respectively. Assuming orthonormal mode shapes $\mathbf{\Phi}$ and proportional damping the modal mass $\mathbf{M}_{\mathrm{m}}$, modal damping $\mathbf{D}_m$ and modal stiffness matrix $\mathbf{K}_m$ of equation (71) simplify to

$$\mathbf{M}_{\mathrm{m}} = \mathbf{\Phi}^T \cdot \mathbf{M} \cdot \mathbf{\Phi} = \mathbf{I} \tag{73}$$

$$\mathbf{K}_m = \mathbf{\Phi}^T \cdot \mathbf{K} \cdot \mathbf{\Phi} = \mathbf{\Omega}^2 = diag(\omega_i^2) \tag{74}$$

$$\mathbf{D}_m = \mathbf{\Phi}^T \cdot \mathbf{D} \cdot \mathbf{\Phi} = \mathbf{Z} \cdot \mathbf{\Omega} = diag(2 \cdot \xi_i \cdot \omega_i) \tag{75}$$

where ω_i is the eigenfrequency of the mode i while $\xi_i \cdot \omega_i$ is the modal damping δ_i. Performing a Laplace transformation of the equations (73) and (74) one obtains the transfer matrix $\mathbf{H}(\omega)$.

$$\mathbf{H}(\omega) = \hat{\mathbf{C}}_m \cdot [-\mathbf{I} \cdot \omega^2 + j \cdot diag(2 \cdot \xi_i \cdot \omega_i) \cdot \omega + diag(\omega_i^2)]^{-1} \cdot \hat{\mathbf{B}}_m \tag{76}$$

By matrix inversion and multiplication the transfer matrix $\mathbf{H}(\omega)$ can be written as

$$\mathbf{H}(\omega) = \sum_{i=1}^{n} \frac{\hat{\mathbf{c}}_i^m \cdot \hat{\mathbf{b}}_i^m}{\omega_i^2 - \omega^2 + 2 \cdot j \cdot \xi_i \cdot \omega_i \cdot \omega} \tag{77}$$

where $\hat{\mathbf{c}}_i^m$ is the modal input vector of the mode i while $\hat{\mathbf{b}}_i^m$ is the modal output vector. For the beam problem with one actuating and one sensing patch equation (77) is reduces to

$$H(\omega) = \sum_{i=1}^{n} \frac{\hat{c}_i^m \cdot \hat{b}_i^m}{\omega_i^2 - \omega^2 + 2 \cdot j \cdot \xi_i \cdot \omega_i \cdot \omega} \tag{78}$$

where $\hat{c}_i^m$ and $\hat{b}_i^m$ correspond to the modal voltage $V_i(x,t)$ and the modal work $\tilde{N}_i(x,t)$ respectively. Following the discussion of the previous sections 8, 9 and 10 the FRF of the simple beam model given by equation (78) can be enhanced by the feedthrough K_D, the effective coupling factor K_{eff} and the residual mode $K_R(\omega)$ which can be expressed as

$$H(x_{pa}, x_{ps}, \omega) = K_{eff}^2 \cdot \left[\sum_{i=1}^{n} \frac{N_i(x_{pa}) \cdot V_i(x_{ps})}{\omega_i^2 - \omega^2 + 2 \cdot j \cdot \xi_i \cdot \omega_i \cdot \omega} + K_D \right] + K_R(\omega) \tag{79}$$

where x_{pa} and x_{ps} are the positions of the actuating and sensing patch respectively.

12 Experimental Verification

In the following the FRFs are verified using a cantilever beam as shown in Figure 1 and described in the section 2. The experimental setup is given in Figure 9. The actuating patch is driven by white noise generated by the measurement hardware (HW) platform (Onosokki, DS-2000). The signal is amplified to 20Volt route mean square (Vrms) by an audio voltage amplifier (KME, SPA 3200MP) and a 50 Volt DC offset is added by a DC power supply (Gossen Konstanter, 14K60R). The voltage applied to the actuating patch is measured by a differential probe (Testec, SI-50) and is used as reference channel for the measurement HW platform. The generated piezoelectric voltages of the sensing patches are used as sensor signals. The FRFs are determined by averaging the response of 100 single measurements.

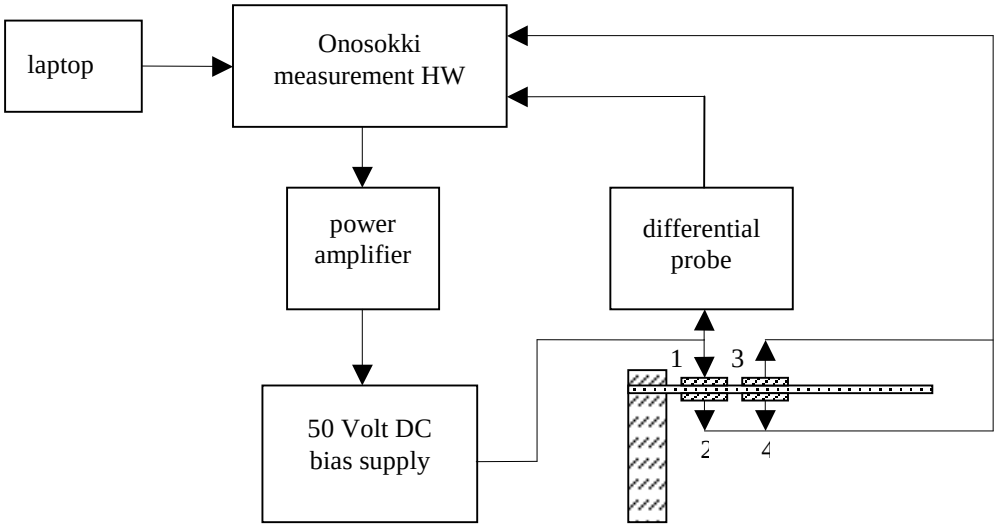

Figure 9. Experimental setup

12.1 Damping Ratio

The damping ratio ξ_i is calculated by a procedure based on the real part of the measured FRFs. It is described in detail in a companion paper (Dennerlein et. al., accepted). The influence of the limited frequency resolution f_{res}^{meas} of the experimental FRFs on the algorithm is investigated by means of error estimation. The experimental frequency resolution f_{res}^{meas} is determined such that the error estimation indicates a worst case error less than 2%. The values used for the different frequency ranges are listed in Table 2.

frequency range	<50Hz	<400Hz	<1600Hz	<5000Hz
f_{res}^{meas} [Hz]	0.0078	0.0625	0.25	0.78

Table 2. Experimental frequency resolutions

The computed damping ratio ξ_i, reported in Table 3, varies from 1.1‰ to 5.1‰. In particular the damping ratio ξ_i of the first bending and longitudinal mode takes the large value 3.1‰ and 5.1‰ respectively whereas the damping ratio ξ_i of the remaining modes takes values between 1.1‰ and 1.6‰. In general the structure is only lightly damped.

12.2 Eigenfrequencies

The eigenfrequencies f_i of the beam are inferred from the measured FRFs. To do so the resonance frequencies f_i^{mag} of the FRFs are identified by a search algorithm implemented in software (SW) (Matlab). Subsequently the eigenfrequencies f_i are calculated based on the resonance frequencies f_i^{mag} and the damping ratio ξ_i.
Following the results of the vibration analysis in section 3.2 and 4.2 the analytical eigenfrequencies f_i are computed. Moreover a FE model of the beam is developed based on 3-dimensional finite elements including the patches with their fully coupled electromechanical fields. The finite element software COSAR (see www.femcos.de) was used to carry out the simulations as well as the calculation of the FRFs.

The experimental, analytical and numerical (FE model) eigenfrequencies f_i are listed in Table 3. The three sets of eigenfrequencies match very well such that the error is less than 0.5% both for the analytical and FE model. The only exemptions with errors of -7.3% and -4.5% for the analytical model and of 3.53% and –5.24% for the FE model are the first bending and longitudinal mode respectively.

	experimental		analytical model		FE model	
mode	f_i [HZ]	ξ_i [‰]	f_i [Hz]	error [%]	f_i [Hz]	error [%]
0. bending xz	19.4	3.1	18.0	-7.3	20.1	3.5
1. bending xz	113.4	1.3	112.9	-0.5	113.5	0.1
2. bending xz	314.8	1.3	316.2	0.4	314.0	-0.3
3. bending xz	611.5	1.1	619.5	1.3	608.7	-0.5
4. bending xz	1025.1	1.3	1024.1	-0.1	1021.0	-0.4
5. bendingx z	1536.1	1.3	1529.9	-0.4	1530.9	-0.3
6. bending xz	2135.1	1.3	2136.8	0.1	2129.9	-0.2
7. bending xz	2857.8	1.5	2844.9	-0.5	2851.2	-0.2
8. bending xz	3668.7	1.2	3654.1	-0.4	3658.3	-0.3
0. longitudinal x	4380.3	5.1	4182.5	-4.5	4162.1	-5.2
9. bending xz	4590.8	1.6	4564.4	-0.6	4584.8	-0.1

Table 3. Eigenfrequencies, damping ratio and modelling error of eigenfrequencies

These results correspond very well to the work of Maxwell and Asokanthan (2004), where the influence of distributed patch arrangements on the mode shapes and on the natural frequencies of a cantilever beam is investigated. They showed that the increase in the eigenfrequency f_i of the first bending mode is several times larger than for the other modes compared to the bare beam.

12.3 Feedthrough, Effective Coupling Factor and Residual Mode

The values for the feedthrough K_D, the effective coupling factor K_{eff} and the residual mode K_R are listed in Table 4. The feedthrough K_D is calculated analytically, see section 8, while the effective coupling factor K_{eff} and the residual mode K_R are found by minimizing the mean absolute modelling error of the analytical FRFs H_{ana} with respect to the measured FRFs H_{meas} in the range from 15Hz to 3 kHz. The error is calculated by

$$error(K_{eff}, K_R) = \frac{1}{2 \cdot \pi \cdot (3000 - 15)} \cdot \int_{2 \cdot \pi \cdot 15}^{2 \cdot \pi \cdot 3000} 20 \cdot |\log(|H_{meas}(\omega)|) - \log(|H_{ana}(K_{eff}, K_R, \omega)|)| \, d\omega \qquad (80)$$

	patch combination			
	1 to 2	3 to 4	1 to 3	2 to 4
feedthrough K_D	0.033	0.033	---	---
effective coupling factor K_{eff}	0.86	0.84	0.81	0.85
residual mode K_R	-0.0080	-0.0050	0.0009	0.0007

Table 4. Feedthrough K_D, effective coupling factor K_{eff} and residual mode K_R

The feedthrough is computed analytically to 0.033, see Table 4. A comparison of the FRF of a simple beam model considering only the modal input and output gains of the patches and of a beam model enhanced by the feedthrough K_D is presented in Figure 10. Looking at e.g. point 1 we can see that the feedthrough K_D increases the amplitude but does not change the position of the resonances. Moreover the feedthrough K_D strongly influences the general slope of the FRFs by shifting the position of the anti-resonances to lower frequencies, see Figure 10 e.g. point 2. Incorporating the feedthrough K_D thus considerably improves the correspondence of analytical and measured anti-resonances such that the average modelling error of the analytical FRFs is reduced from about 10.8dB to about 6dB, see Table 5.

The model used for the induced strain analysis in section 7 considered only the pure piezoelectric layer neglecting the bonding layer, the electrodes and the embedding polymer matrix of the patches. Thus the feedthrough is slightly overestimated and the analytical anti-resonances are shifted too far to lower frequencies such that they are positioned to the left of the measured ones, see Figure 10 e.g. point 2.

	modelling error [dB] for patch combination			
	1 to 2	3 to 4	1 to 3	2 to 4
simple model	10.4	11.1	5.1	4.2
simple model with K_D	6.5	5.4	---	---
simple model with K_D and K_{eff}	1.5	1.4	2.9	2.3
simple model with K_D, K_{eff} and K_R	0.9	1.3	2.5	2.0

Table 5. Modelling error of the analytical FRFs

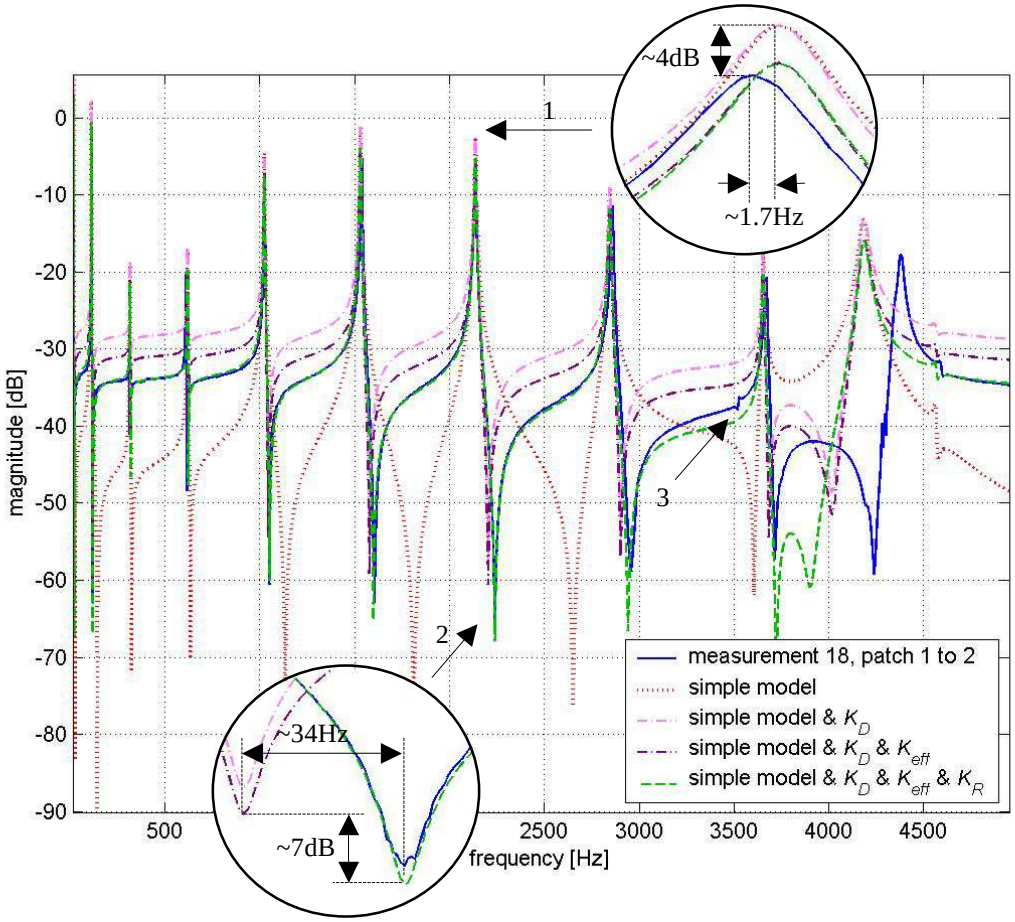

Figure 10. Collocated FRFs of the stepwise enhanced analytical beam model

The estimated effective coupling factor K_{eff}, given in Table 4, depends on the patch combination used and varies between 0.81 and 0.86 due to the individual mechanical, electrical or thermal aging and manufacturing tolerances of the single patches. This is within the range of deviation that can be expected by the above mentioned aging rates and manufacturing tolerances.

The FRF of a beam model enhanced by the feedthrough K_D and the effective coupling factor K_{eff} is shown in Figure 10. Including the effective coupling factor K_{eff} in the beam model shifts the FRF by

$$20 \cdot \log_{10}(K_{eff}^2) \tag{81}$$

in the complete frequency range with respect to the beam model enhanced only by the feedthrough K_D. The average modelling error of the analytical FRFs decreases to about 1.5dB for the collocated and to about 2.5dB for the non-collocated patch combinations, see Table 5.

Similar to the effective coupling factor K_{eff} the deferred residual mode K_R, listed in Table 4, depends on the patch combination. It extends over the range from -0.0080 to 0.0009 as a result of the different modal input and output gains of the truncated modes associated with the single patch locations.
Finally the FRF of a beam model enhanced by the feedthrough K_D, the effective coupling factor K_{eff} and the residual mode K_R is shown in Figure 10. Like the feedthrough K_D the residual mode K_R contributes to the amplitude but does not change the position of the resonances, see Figure 10 e.g. point 1. The residual mode K_R mainly affects the general slope of the FRFs improving the correspondence of the measured and the analytical anti-resonances, see Figure 10 e.g. point 2. Incorporating the residual mode K_R in the beam model minimizes the average modelling error of the analytical FRFs to about 1.2dB for the collocated and to about 2.2dB for the non-collocated patch combinations, see Table 5.

12.4 Frequency Response Function

The observed modelling error of the analytical FRFs, listed in Table 5, is greatly reduced by the improvement of the simple beam model with the feedthrough K_D, the effective coupling factor K_{eff} and the residual mode K_R. The biggest reduction in the modelling error is achieved by the feedthrough K_D followed by the effective coupling factor K_{eff}. The residual mode K_R contributes only with a small decrease in modelling error.

It is pointed out that the minimum modelling error of about 1.2dB for the collocated and 2.2dB for the non collocated patch combinations, listed in Table 5, is achieved only by means of combining all three additional modelling techniques. Though the cantilever beam is regarded to be just a simple one-dimensional structure high quality analytical FRFs are only obtained by the use of advanced modelling techniques requiring a thorough understanding of the main behaviour of smart structures.

The FRFs obtained by measurement, analytical and numerical simulations are compared in Figure 10 and in Figure 11 for a collocated and a non-collocated patch combination respectively. The corresponding patch numbering is explained in Figure 1 and the experimental setup is described in Figure 9.

The analytical FRFs nearly match the measured ones in the frequency range up to 3.6 kHz both for the collocated and the non-collocated patch combinations. Larger discrepancies are noted only in the presence of unintentionally excited torsional modes of the x axis and bending modes of the xy plane, see e.g. Figure 10 e.g. point 3 and Figure 11 e.g. points 1 and 2. The torsional modes may be excited due to not symmetrically mounted patches, local inhomogeneities or manufacturing tolerances of the beam substrate or of the patches.

The measured FRFs of the patch combinations 1 to 2 and 2 to 4 hardly contain any unintentionally excited modes such that the achieved modelling error is about 0.4dB smaller compared to the modelling error of the FRFs of the similar patch combinations 3 to 4 and 1 to 3, see Table 5.

Comparing the analytical, numerical and experimental eigenfrequencies f_i one can see that the eigenfrequencies of the FE model correspond better to the measured ones, see Table 3. With respect to the plots no difference can be noticed, see Figure 11. In general the slope of the numerical FRFs agrees less with the experimental data. This might be due to the residual mode that has not been included in the finite element model.

The extremely low modelling error of the analytical FRFs and the excellent matching of the analytical and measured FRFs make the presented analytical beam model especially suited for further analysis like patch placement and compensator design or the development and test of advanced numerical analysis tools such as the finite element method and the controller design (Nestorovic-Trajkov et. al., 2005).

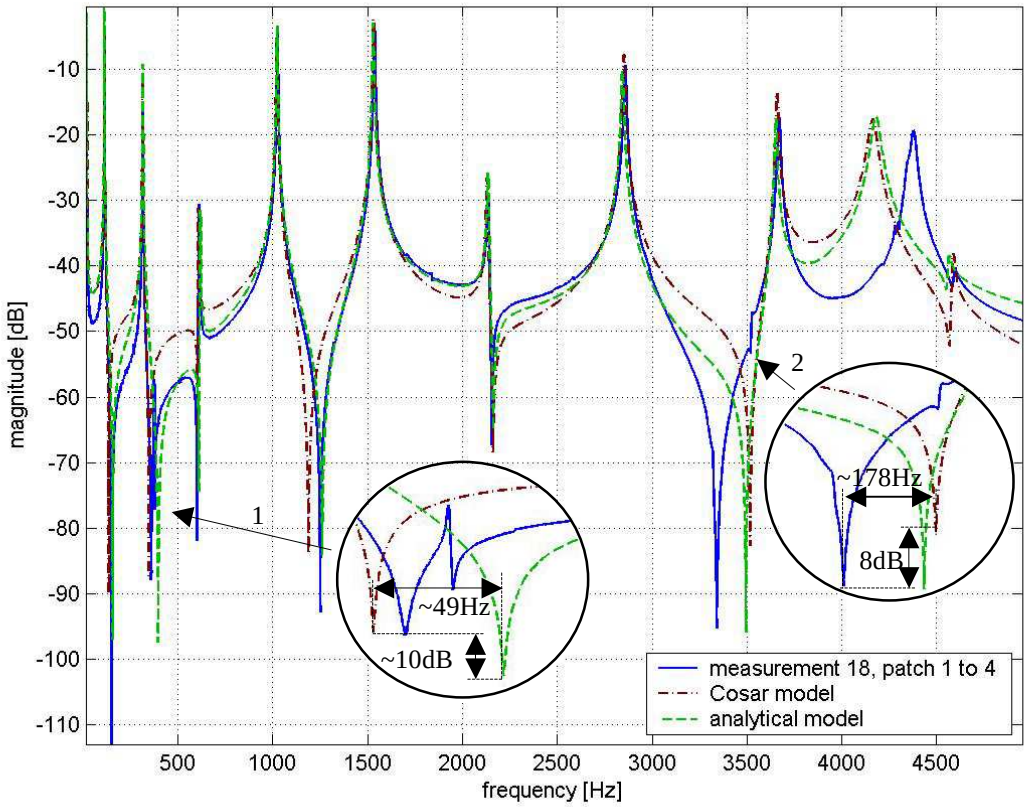

Figure 11. Non-collocated FRFs of the COSAR and proposed analytical model

13 Conclusion

An enhanced analytical beam model has been proposed in the presented paper. The traditional analytical Euler-Bernoulli model of the bending vibrations has been combined with a model of the longitudinal vibrations. The effects of mechanical coupling of actuators and collocated sensors, of effective piezoelectric coupling and of model truncation have been formulated analytically and have been incorporated in the model. Analytical and measured FRFs have been presented and show excellent agreement. The study not only offers an enhanced beam model but extends the verification of the theory up to highest modal orders.
It has been concluded that the beam is sufficiently complex to develop a thorough understanding of smart structures. In addition, both analytical and numerical methods can be used for further investigations regarding patch placement and compensator development.

14 References

Alberts, T. E.; DuBois, T. V.; Pota, H. R.: Experimental verification of transfer functions for a slewing piezoelectric laminate beam. *Control Engineering Practice*, **3**, 2 (1995), 163-170.

Alvarez-Salazar, O. S.; Iliff, K.: Destabilizing effects of rate feedback on strain actuated beams. *Journal of Sound and Vibration*, **221**, 2 (1999), 289-307.

BMBF Leitprojekt Adaptronik. Förderkennzeichen 03 N 8500 - 17, Braunschweig: DLR Braunschweig, (1998).

CeramTec, *Piezoceramics,* 2006, http://www.ceramtec.com/pdf/piezoceramics.pdf.

Crawley, E. F.; Anderson, E. H.: Detailed models of piezoceramic actuation of beams. *Journal of Intelligent Material Systems and Structures*, **1**, (1990), 4-25.

Crawley, E. F.; de Luis, J.: Use of piezoelectric actuators as elements of intelligent structures. *American Institute of Aeronautics and Astronautics Journal*, **25**, 10, (1987), 1373-1385.

Dennerlein, J.; Gabbert, U.; Köppe, H.; Nunninger, S.; Bechtold, M.: Structural modal parameter estimation with collocated piezoelectric patch actuators and sensors. *Proceedings of the Eight International Conference on Computational Structures Technology*, Las Palmas de Gran Canaria, Spain, September 12-15, 2006, Civil-Comp Press, Stirling, United Kingdom, accepted.

Edery-Azulay, L.; Abramovich, H.: Active damping of piezo-composite beams. *Composite Structures,* accepted.

Fuller, C. R.; Elliott, S. J.; Nelson, P. A.: *Active control of vibration,* London: Academic Press, (1997).

Gabbert, U.: Research activities in smart materials and structures and expectations to future developments. *Journal of Theoretical and Applied Mechanics*, **40**, 3, (2002), 549-574.

Gabbert, U.; Berger, H.; Köppe, H.; Xao, C.: On modelling and analysis of piezoelectric smart structures by the finite element method. *Journal of Applied Mechanics and Engineering*, **5**, 1, (2000), 127-142.

Gao, Y. R.; Randall, B.: Determination of frequency response functions from response measurements--II. Regeneration of frequency response from poles and zeros. *Mechanical Systems and Signal Processing*, **10**, 3, (1996), 319-340.

Görnandt, A.; Gabbert, U.: Finite element analysis of thermopiezoelectric smart structures. *Acta Mechanica*, **154**, 1-4, (2002), 129-140.

Kusculuoglu, Z. K.; Fallahi, B.; Royston, T. J.: Finite element model of a beam with a piezoceramic patch actuator. *Journal of Sound and Vibration*, **276**, 1-2, (2004), 27-44.

Maxwell, N. D.; Asokanthan, S. F.: Modal characteristics of a flexible beam with multiple distributed actuators. *Journal of Sound and Vibration*, **269**, 1-2, (2004), 19-31.

Meyers, A., *Maschinendynamik,* Ruhr-Universität Bochum, Maschinenbau, (2005).

Nestorovic-Trajkov, T.; Köppe, H.; Gabbert, U.: Active vibration control using optimal LQ tracking system with additional dynamics. *International Journal of Control*, **78**, 15, (2005), 1182-1197.

Nguyen, C. H.; Pietrzko, S. J.: Piezoelectric-mechanical-acoustic couplings from a PZT-actuated vibrating beam and its sound radiation. *Mechanical Systems and Signal Processing*, **18**, 4, (2004), 929-945.

PI Ceramic GmbH, *Application Notes,* 2005b, http://www.piceramic.com/site/picomp_004.html.

PI Ceramic GmbH, *Piezoceramic Materials,* 2005a, http://www.piceramic.com/pdf/piezo_material.pdf.

Pota, H. R.; Alberts, T. E.: Multivariable transfer functions for a slewing piezoelectric laminate beam. *Journal of Dynamic Systems, Measurement and Control*, **117**, (1995), 352-359.

Preumont, A.: *Vibration control of active structures: an introduction*, Kluwer Academic Publisher, (2002).

Randall, R. B.; Gao, Y.: Extraction of modal parameters from the response power cepstrum. *Journal of Sound and Vibration*, **176**, 2, (1994), 179-193.

Stöbener, U.: *Untersuchungen zur Schwingungs- und Schallabstrahlungsregelung flächenhafter Strukturen.* Düsseldorf: VDI-Verlag, (2002).

Wang, B. -T.: Structural modal testing with various actuators and sensors. *Mechanical Systems and Signal Processing*, **12**, 5, (1998), 627-639.

Addresses: Dipl.-Ing. Jürgen Dennerlein, Prof. Dr.-Ing. Ulrich Gabbert and Dr.-Ing. Heinz Köppe, Institut für Mechanik, Otto-von-Guericke-Universität Magdeburg, Universitätsplatz 2, D-39106 Magdeburg; Dipl.-Ing. Stefan Nunninger and Dipl.-Ing. Mario Bechtold, Siemens AG, Bereich Corporate Technology, Günther-Scharowsky-Str. 1, 91050 Erlangen.
email: juergen.dennerlein@web.de; ulrich.gabbert@mb.uni-magdeburg.de;
heinz.koeppe@mb.uni-magdeburg.de; stefan.nunninger@siemens.com; mario.bechtold@siemens.com